Holey Graphitic Carbon Nitride Nanosheets with Carbon Vacancies for Highly Improved Photocatalytic Hydrogen Production

Qinghua Liang, Zhi Li, Zheng-Hong Huang, Feiyu Kang, and Quan-Hong Yang**

2D graphitic carbon nitride (GCN) nanosheets have attracted tremendous attention in photocatalysis due to their many intriguing properties. However, the photocatalytic performance of GCN nanosheets is still restricted by the limited active sites and the serious aggregation during the photocatalytic process. Herein, a simple approach to produce holey GCN (HGCN) nanosheets with abundant in-plane holes by thermally treating bulk GCN (BGCN) under an NH_3 atmosphere is reported. These formed in-plane holes not only endow GCN nanosheets with more exposed active edges and cross-plane diffusion channels that greatly speed up mass and photogenerated charge transfer, but also provide numerous boundaries and thus decrease the aggregation. Compared to BGCN, the resultant HGCN has a much higher specific surface area of 196 $m^2 g^{-1}$, together with an enlarged bandgap of 2.95 eV. In addition, the HGCN is demonstrated to be self-modified with carbon vacancies that make HGCN show much broader light absorption extending to the near-infrared region, a higher donor density, and remarkably longer lifetime of charge carriers. As such, HGCN has a much higher photocatalytic hydrogen production rate of nearly 20 times the rate of BGCN.

1. Introduction

The increase of environmental pollution and the depletion of fossil resources have resulted in an ever-growing demand for green and unlimited solar energy, and this has triggered an enormous amount of research on the development of highly efficient photocatalysts under the current global background of the increase in environmental pollution and the depletion of fossil resources.[1] Since the pioneering work in 2009,[1c,2] graphitic carbon nitride (GCN), as a significant photocatalyst, is of tremendous interest due to its many extraordinary features, such as its environmental benignity, good thermal and chemical stability, cost effectiveness, metal-free composition, and easy preparation.[1c,3] However, a low specific surface area (SSA), insufficient solar-light absorption, and fast recombination of photogenerated electrons and holes caused by the π–π conjugated electronic system severely limit the photocatalytic performance of conventional bulk GCN (BGCN).[1d,3] In this context, considerable and continuing effort has been devoted to improve the activity of GCN-based photocatalysts over the past six years.

So far, the strategies proposed to address the above drawbacks of GCN can be mainly classified into two categories. One way is optimizing the electron and bandgap structures by introducing functional groups,[4] doping with heteroatoms,[5] modifying with nitrogen vacancies,[6] or constructing heterojunctions with other semiconductor materials.[7] Another approach is the development of various GCN nanostructures with optimized physicochemistry and optical properties, including nanoparticles,[8] nanosheets,[1g,9] nanorods,[10] nanoribbons,[11] nanotubes,[12] nanospheres,[1e,13] "seaweed,"[14] etc. In particular, much attention has been paid to 2D GCN nanosheets because of their enlarged SSA, strikingly improved electron–phonon interaction, and enhanced electron mobility along the in-plane direction.[1g,9,15] However, the amount of photocatalytic active sites in GCN nanosheets is still confined due to the limited boundaries and exposed edges. In addition, the van der Waals attraction and π–π stacking between GCN nanosheets cause serious aggregation and restacking, and thus limit the transport of the H_2O_2 intermediate product which often poisons GCN during the photocatalytic process,[1d] leading to poor recycling

Q. Liang, Prof. Z.-H. Huang, Prof. F. Kang
State Key Laboratory of New Ceramics and Fine Processing
School of Materials Science and Engineering
Tsinghua University
Beijing 100084, P. R. China
E-mail: zhhuang@tsinghua.edu.cn

Q. Liang, Prof. F. Kang, Prof. Q.-H. Yang
Shenzhen Key Laboratory for Graphene-Based Materials and Engineering Laboratory for Functionalized Carbon Materials
Graduate School at Shenzhen
Tsinghua University
Shenzhen 518055, P. R. China
E-mail: yang.quanhong@sz.tsinghua.edu.cn

Q. Liang, Prof. Z. Li
Technical Institute of Physics and Chemistry
Chinese Academy of Sciences (CAS)
Beijing 100190, P. R. China

Prof. Z.-H. Huang, Prof. F. Kang
Key Laboratory of Advanced Materials (MOE)
School of Materials Science and Engineering
Tsinghua University
Beijing 100084, P. R. China

Prof. Q.-H. Yang
School of Chemical Engineering and Technology
Tianjin University
Tianjin 300072, P. R. China

DOI: 10.1002/adfm.201503221

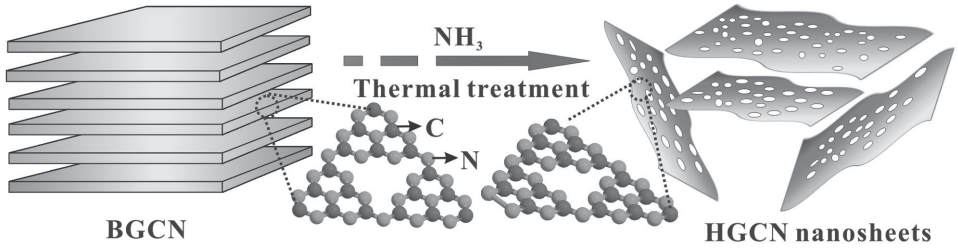

Figure 1. Illustration of the preparation process of HGCN nanosheets. The insets are their possible structures (arrows indicate C atoms and N atoms).

performance. It has been demonstrated that making porous structure in GCN nanosheets can greatly alleviate the above pro blem.[9a,d,15b,16] Most recently, we have also reported a macroscopic 3D GCN monolith constructed with porous nanosheets for improved photocatalytic hydrogen evolution.[16b] In this case, holey GCN nanosheets (HGCNs), characterized with numerous in-plane holes are more favorable because these opened pores are more accessible and can significantly improve the mass and charge transport across the GCN planes during the photocatalytic process. More importantly, these in-plane holes will not only significantly increase the number of exposed active sites, but also effectively prevent their aggregation by greatly reducing interaction sites. For example, this approach has been demonstrated to be highly effective in improving the catalytic and energy storage performance of graphene-based materials.[17] Although there are many studies concerning the synthesis of GCN nanosheets, the preparation of HGCN nanosheets is still a great challenge.

In this work, we first report an easy approach to prepare HGCN by thermally treating BGCN under an NH_3 atmosphere (**Figure 1**). Using this method, BGCN is effectively exfoliated into nanosheets with abundant in-plane holes. At the same time carbon vacancies are created in the resulting HGCN. The in-plane holes not only endow HGCNs with more boundaries and thus decrease their van der Waals interaction, but also provide numerous new active edges and cross-plane diffusion channels that can greatly speed up mass transfer and the diffusion of photogenerated charge carriers. Furthermore, the carbon vacancies give HGCN a broad light absorption band that extends into the near-infrared (NIR) region, and remarkably reduce the probability of the recombination of photoexcited charge carriers. As expected, HGCN exhibits significantly improved photocatalytic performance than the parent BGCN in hydrogen generation (≈20 fold) under visible light.

2. Results and Discussion

The key of our approach is the temperature at which the BGCN is heated in the NH_3 atmosphere. It should be noted that the diameter and the concentration of holes produced in the HGCNs depend on the heating temperature, heating period, and the ammonia flow. The optimized heating temperature for preparing HGCNs ranges from 490 to 520 °C. The size, thickness, yield, and C/N molar ratio of the HGCNs decrease with increased reaction time (Figure S1 and Table S1, Supporting Information), indicating the gradual decomposition of BGCN into gaseous products during the reaction with NH_3. The released gas assists the expansion of the stacked GCN layers, resulting in the formation of few-layer holey nanosheets. In this study, HGCN obtained by etching BGCN at 510 °C for 1 h was particularly studied unless otherwise specified.

Low-magnification scanning electron microscope (SEM) images (**Figure 2**A,B) show that the resultant HGCNs are highly corrugated with a thickness about 20 nm. The edges of the nanosheets are curled and rough as a result of minimizing the surface energy.[1g] A high-magnification SEM image clearly reveals their holey structure with abundant in-plane holes with diameters ranging from tens to hundreds of nanometers (insets in **Figure 3**A,B). Transmission electron microscope (TEM) images (Figure 2C) confirm that the HGCNs are laminar and contain many holes. A large number of in-plane holes of a few nanometers diameter can be clearly seen (Figure 2D), in agreement with the SEM observation. A selected area electron diffraction (SAED) pattern of the HGCNs (inset in Figure 2C) shows two diffraction rings indexed to the (100) and (002) planes of hexagonal GCN, suggesting their polycrystalline nature.[18] A high-resolution TEM image also clearly shows many nanoholes and distorted lattice fringes (Figure S2, Supporting Information), indicating the presence of vacancies. These nanoholes and the distorted atomic arrangement cause the rupture of the nanosheets and thus result in additional phototcatalytic active sites.

The pore structure and SSA of the HGCN are obtained from the N_2 adsorption–desorption measurements at 77 K. As shown in Figure 3A, HGCN exhibits a type-IV isotherm with an extremely high adsorption capacity in the high relative pressure (P/P_0: from 0.85 to 1), suggesting the presence of abundant mesopores and macropores. The Brunauer–Emmett–Teller SSA of HGCN is calculated to be ≈196 $m^2\ g^{-1}$, which is 32.6 times higher than that of BGCN (≈6 $m^2\ g^{-1}$). Correspondingly, HGCN possesses a much larger pore volume compared to BGCN. The total pore volume of HGCN is ≈1.38 $cm^3\ g^{-1}$ as defined at $P/P_0 = 0.99$, which is ≈23 times higher than that of BGCN (≈0.06 $cm^3\ g^{-1}$). Note this value is among the highest values ever reported for nanostructured GCN materials.[8b,19] The extremely high pore volume may result from a large number of in-plane holes and the crumpled structure. To further analyze the pore structure of HGCN, pore size distribution (PSD) plots were obtained using the Barrett–Joyner–Halenda method. The PSD curve of HGCN has a sharp peak at 4 nm and a broad distribution in the range of 20–100 nm, while that of BGCN shows negligible peaks. The high SSA and large pore volume result in a much larger volume of HGCN with the same weight as BGCN (Figure 3B), and may effectively promote the kinetics of the photocatalytic reaction by facilitating mass transfer.

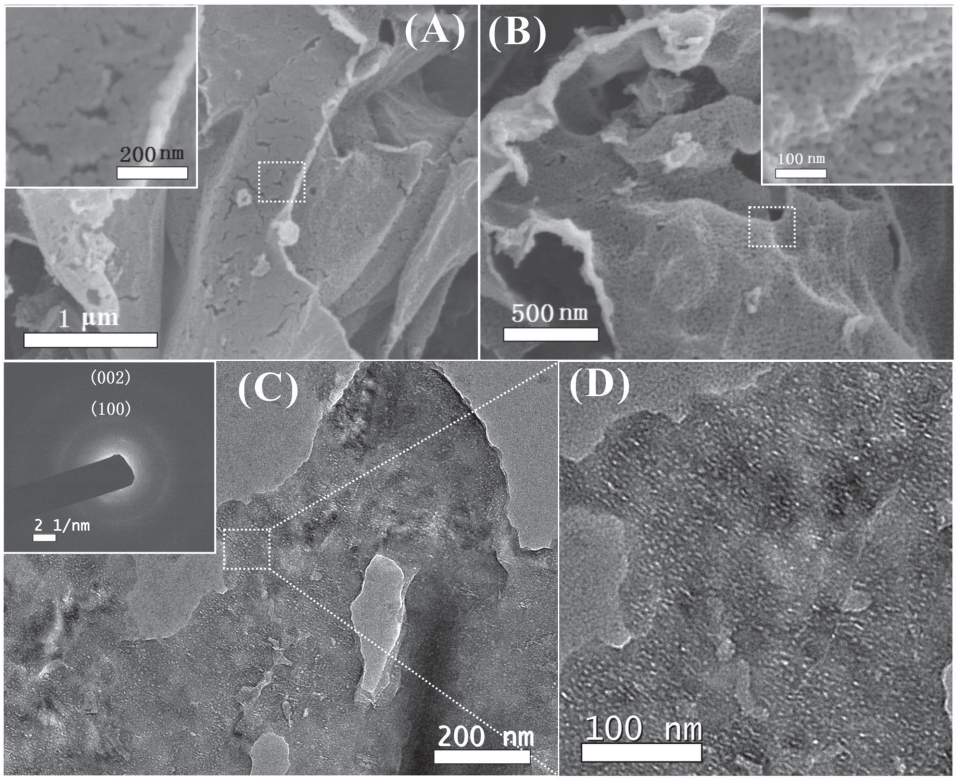

Figure 2. A,B) Typical SEM and C,D) TEM images of HGCN nanosheets. The inset in panel (C) is the corresponding SAED pattern.

The crystal structure of the HGCN was studied by X-ray diffraction (XRD). Compared to the parent BGCN, the two peaks at 13.1° (100) and 27.4° (002), which are respectively ascribed from the in-plane trigonal nitrogen linkage of tri-s-triazine motifs and the periodic stacking of layers of conjugated aromatic systems (inset in Figure 3C),[1g,20] have a much reduced intensity and are broader. This mainly results from the reduced length of interlayer periodicity and a larger spacing between the HGCN layers.[21] Fourier transform infrared (FTIR) spectra of both BGCN and HGCN (Figure 3D) show broad peaks assigned to amine groups or water between 2900 and 3600 cm^{-1}, characteristic stretching modes of CN heterocycles from 1200 to 1600 cm^{-1}, and a typical breathing mode of the triazine units at ≈810 cm^{-1}, revealing their similar chemical structures. [1e,16b,20,22] All the peaks of HGCN are sharper than those of BGCN, which is caused by the more ordered packing of tri-s-triazine motifs in the nanosheets.[1g,9b]

The chemical compositions and elemental valence states were investigated by elemental analysis and X-ray photoelectron spectroscopy (XPS). As compared in **Figure 4**E, XPS survey spectra of both BGCN and HGCN contain three sharp peaks at 288, 399, and 532 eV, which are respectively assigned to C 1s, N 1s, and O 1s signals. Note that the O 1s signal may be from the absorbed CO_2 and H_2O on the surface of the samples. Quantitative analysis from XPS reveals that the C/N molar ratio of HGCN (0.68) is much smaller than that of BGCN (0.76). Elemental analysis (Table S1, Supporting Information) also shows that the HGCN has a smaller C/N atomic ratio (0.66) than that of BGCN (0.72), suggesting the presence of carbon vacancies in HGCN (Figure S3, Supporting Information). The creation of carbon vacancies may be attributed to the reaction between some carbon species of GCN with ammonia at high temperature.[23] Considering many different types of carbon species in GCN, further mechanistic study is undergoing to verify this assumption. The C 1s and N 1s spectra are almost the same for both BGCN and HGCN (Figure 4F), further indicating that NH_3 etching has little influence on the CN aromatic systems. However, an increase in the intensities of both the C 1s and N 1s spectra of HGCN is clearly observed because C and N atoms neighboring carbon vacancies get fewer electrons than those on the normal sites (Figure 3E and Figure S3, Supporting Information). The C 1s spectrum can be resolved into two peaks centered at 288.5 and 285.0 eV, which are respectively attributed to C=C and N–=C–N bonds.[3a,9b,24] The peak-area ratio of N=C–N to C=C increases from 0.13 to 0.14 in HGCN, indicating the loss of graphitic carbon species during the NH_3 etching process. Fewer graphitic carbon species can suppress the charge recombination, and carbon vacancies may increase the electrical conductivity and the mobility of photogenerated charge carriers.[22] Moreover, four peaks centered at binding energies of 398.6, 399.4, 400.8, and 404.6 eV are obtained after deconvolution of the N 1s spectra, and these are respectively attributed to N species in N=C–N, N–$(C)_3$, N–H, and positive charge localization in heptazine rings.[3a,9b,24] Compared to BGCN, the peak-area ratio of N=C–N increases from 0.45 to 0.50 in HGCN (Figure S3, Supporting Information), suggesting the possible transformation of C=C to N=C after NH_3 treatment.

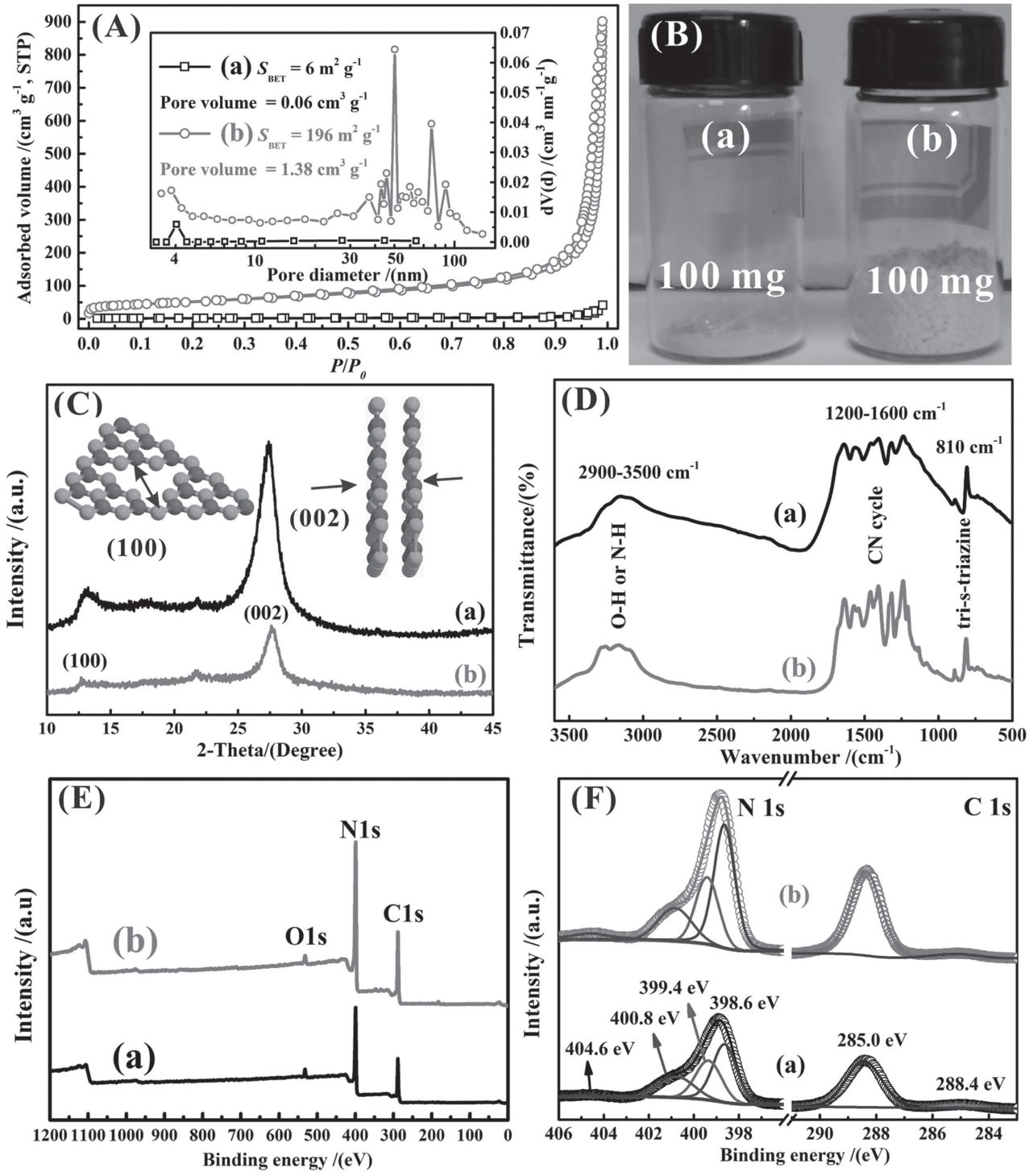

Figure 3. A) N_2 adsorption–desorption isotherms at 77 K and the corresponding PSD curves (inset), B) photograph of 100 mg powder, C) XRD patterns, D) FTIR spectra, E) XPS survey spectra, and F) high resolution C 1s and N 1s XPS spectra of a) BGCN and b) HGCN.

It is expected that these unique holey nanosheets containing carbon vacancies would have a large effect on the optical properties of HGCN. We studied their optical properties by UV–vis absorption and photoluminescence (PL) spectroscopy. Compared with BGCN, the absorption edge of HGCN is blue shifted from ≈480 to ≈430 nm. Furthermore, a broader and stronger absorption tail, starting at ≈530 nm and extending to the NIR region (800–1400 nm), is also clearly observed (Figure 4A), which thus gives HGCN the grey color (Figure 3B). The increased optical absorption of HGCNs in the

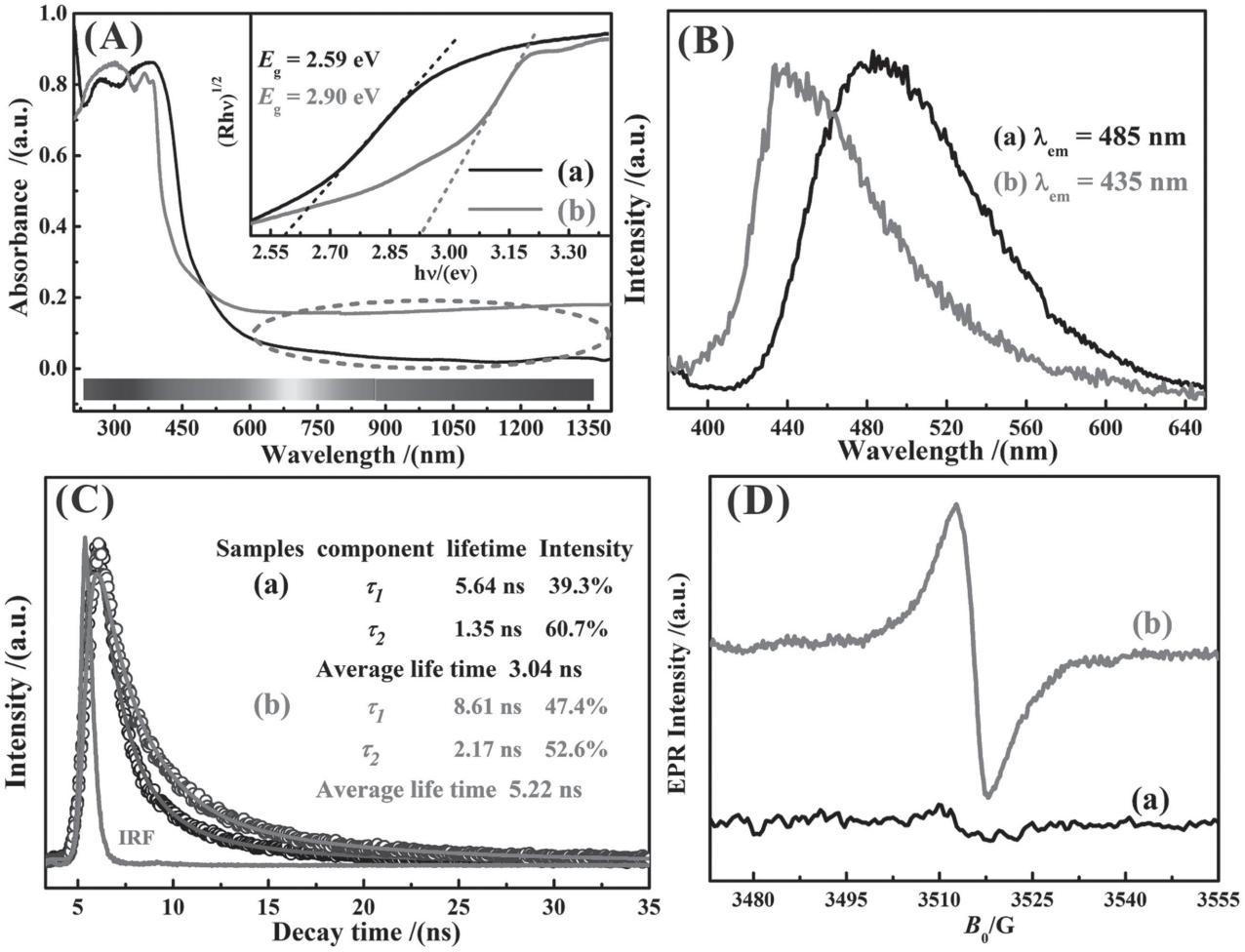

Figure 4. A) DRS spectra and Tauc plots, B) PL spectra, C) time-resolved PL spectra collected under an excitation of 400 nm, and D) EPR spectra of a) BGCN and b) HGCN.

visible region (≈530–800 nm) may be caused by the multiple reflection of incident light in pores and holes in the structure, and the NIR absorption may be caused by the presence of carbon vacancies. It has been previously reported that carbon vacancies can induce the ferromagnetism in GCN at room temperature owing to spin-polarized conduction electrons in the spin-down branch.[25] Thus, this assumption can be confirmed by the magnetic measurements. An obvious hysteresis hoop is observed in the curve of the magnetic field dependence of the magnetization (*M*–*H*) recorded at 300 K (Figure S4, Supporting Information), confirming the room-temperature ferromagnetism of HGCN. Meanwhile, Tauc plots obtained from the Kubelka–Munk function reveal an increase in the bandgap energy of HGCN to 2.90 eV compared to 2.59 eV for BGCN (inset in Figure 4A), which may be caused by the effect of quantum confinement effect in the nanosheet structure of HGCNs.[1g,9b,c,21]

PL is an effective strategy to characterize the separation and recombination rates of charge carriers of a photocatalyst. Two broad emission peaks centered at ≈485 and ≈435 nm are observed for BGCN and HGCN, respectively, and these are the intrinsic PL emissions with the optical energy close to the bandgap energy (Figure 4B). Meanwhile, a large number of small peaks are also observed in the emission spectrum of HGCNs, suggesting the possible existence of various different emission centers. We further studied the PL decays of HGCN and BGCN to have more information of the charge carriers. The time-resolved PL spectra collected at the wavelength of their maximum emission was compared in Figure 4C. The text included in Figure 4C summarizes the average lifetime and its %contribution determined from a double-exponential fitting. Specifically, the average PL lifetime of HGCN is 1.7 times longer than those of BGCN by altering the contribution of each lifetime. The longer (8.61 ns) and shorter (2.17 ns) lifetimes have the contributions of 47.4% and 52.6%, respectively, to the total PL emission intensity. Both values are significantly different from those of BGCN (5.64 ns, 39.3%, and 1.35 ns, 60.7%), suggesting the obviously different emission pathway. The longer lifetime of intrinsic fluorescence may be associated with the improved transport rate of photocarriers resulting from the quantum confinement effect in the HGCN nanosheets.[1g] Furthermore, it is found that the PL lifetime of HGCN depends on the monitoring signal. For example, the average PL lifetime became much shorter (2.60 ns) when the collecting wavelength

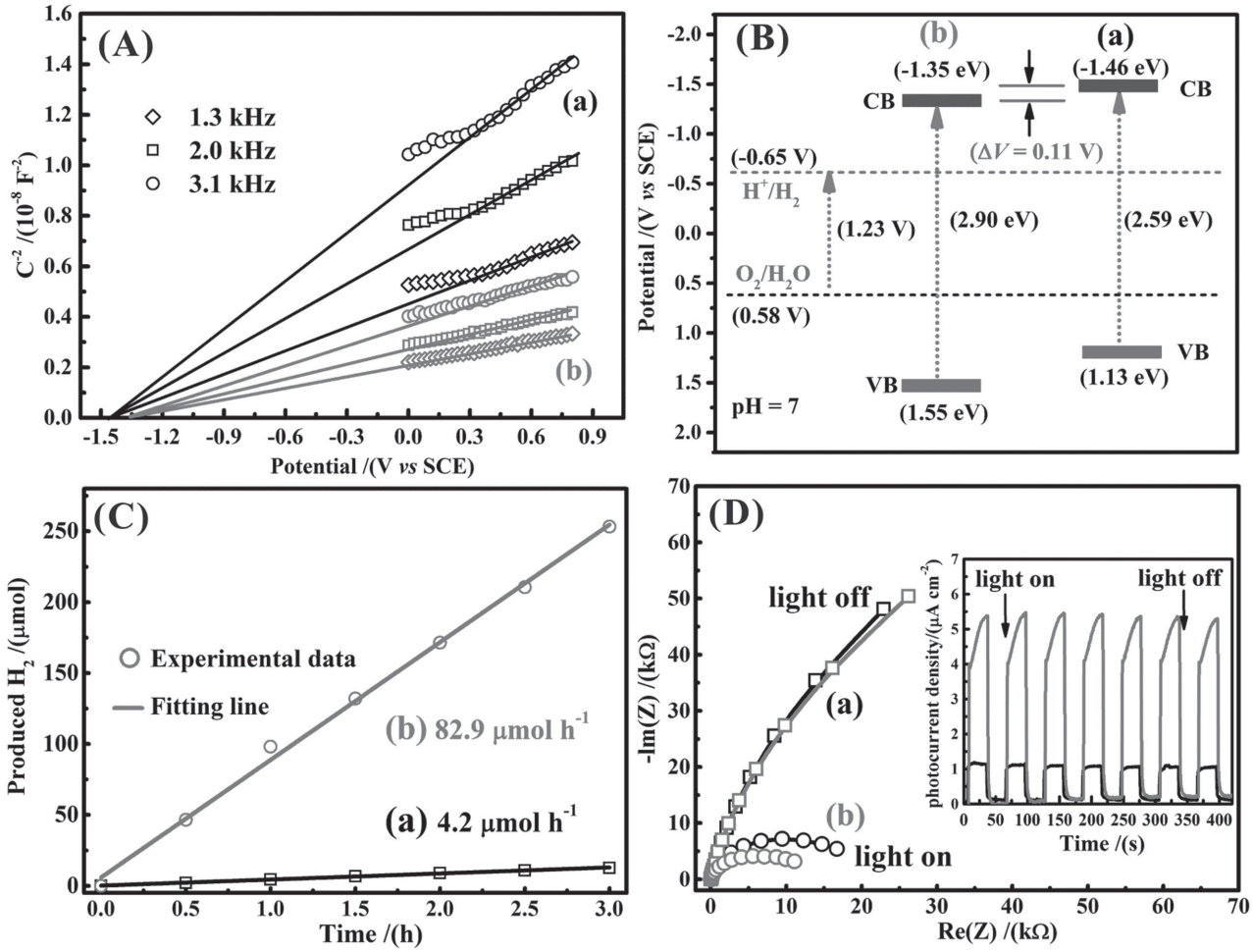

Figure 5. A) Mott–Schottky plots collected at various frequencies, B) bandgap structures, C) photocatalytic H_2 evolution performance, and D) electrochemical impedance spectra and transient photocurrent response (inset) of a) BGCN and b) HGCN nanosheets.

is 485 nm (Figure S5, Supporting Information). The reason may be that the diffusion rate of photoexcited carriers in HGCN is influenced by the defects or disorder and the π–π conjugated electronic systems between interlayers.[26] Furthermore, electron paramagnetic resonance (EPR) measurements at room temperature show that the holey nanosheets have a greater ability to delocalize electrons and thus inhibit the recombination of the photogenerated electrons and holes. As compared in Figure 4D, both BGCN and HGCN exhibit one single Lorentzian line with a *g* value of 2.0036 in a magnetic field from 3400 to 3600 G, and this is induced by a lone electron pair on the carbon atoms of the heptazine rings within p-bonded nanosized clusters.[24,27] However, compared to the parent BGCN, the significantly stronger EPR spin intensity of HGCN reveals the much higher concentration of unpaired electrons, which is very useful for the photogeneration of active radical pairs for catalytic reaction.[24] Such optical properties of HGCN are very beneficial for the photocatalytic process.

In order to make sure that the as-prepared HGCN are suitable for photocatalytic hydrogen evolution under visible light, we studied their electronic band structure by examining of Mott–Schottky plots which refers to the apparent capacitance as a function indifferent frequency ranges compared to BGCN. As shown in **Figure 5**A, both HGCN and BGCN exhibit positive slopes in the Mott–Schottky plots at frequencies of 1.3, 2.0, and 3.1 kHz, which is an indication of the n-type characteristic of semiconductors.[1e,9b,28] The Mott–Schottky plot of HGCN shows a smaller slope than that of BGCN, suggesting a higher electron donor density for HGCNs. A high donor density, possibly caused by carbon vacancies, is very helpful for improving photocatalytic performance because of the increased electrical conductivity and the mobility of charge carriers.[29] The flat band potentials determined as the *x*-intercept in the Mott–Schottky plot of BGCN and HGCN are respectively about −1.35 and −1.46 V with reference to the saturated calomel electrode (SCE). The 0.11 V downshift of the conduction band may be caused by carbon vacancies and the nanosheet structure of HGCN.[9b,25] The lower flat band potential also indicates a higher electrical conductivity of HGCN compared to BGCN.[9b] The potentials of the valance bands of BGCN and HGCN are respectively calculated to be 1.13 and 1.45 eV (Figure 5B) by a combined analysis of bandgaps derived from the DRS spectra (Figure 4A). The potentials of H_2/H^+ and O_2/H_2O with reference to the SCE are also shown in Figure 5B.[5b] It is found that both HGCN and

BGCN satisfy the thermodynamical condition for the photocatalytic splitting of water for hydrogen evolution.

We evaluated the HGCN and BGCN as heterogeneous photocatalysts for water splitting to produce hydrogen production under visible light (λ> 420 nm). As compared in Figure 5C, the hydrogen production rate of HGCN is about 82.9 μmol h^{-1}, which is 20 times higher than that of the BGCN (≈4.2 μmol h^{-1}). The photocatalytic activity of HGCN is also much better than that of the 3D porous graphitic carbon monolith.[16b] Considering that HGCN and BGCN have similar chemical compositions, we assume that the following factors may be responsible for the much greater photocatalytic activities of HGCN. First and foremost, the much higher SSA combined with the unique holey structure provides more exposed active edges, catalytic sites, and channels for the photocatalytic hydrogen evolution reaction. Furthermore, the in-plane holes in HGCN are also beneficial for the rapid cross-plane diffusion of mass, photogenerated carriers, and hydrogen, which dramatically accelerate the photocatalytic reaction in kinetics. Thus, the photocatalytic activity increases with an increasing SSA (Table S1, Supporting Information). Second, based on a combined analysis of DRS and the Mott–Schottky plots, HGCN can absorb more visible and NIR light and thus have a lower flat potential and a higher donor density, which promotes the photocatalytic reaction thermodynamically. Third, HGCN has a significantly improved separation efficiency of photogenerated carriers and a much higher degree of electron delocalization, as indicated by the increased lifetime of PL emission and the stronger EPR intensity (Figure 4C,D). These are also reflected in the greatly increased transient photocurrent and much smaller diameter of the semicircular Nyquist curve of electrochemical impedance spectroscopy under visible light radiation (Figure 5D). Note that the arc radius of the Nyquist plot in the dark for HGCN is smaller than that of BGCN, implying a smaller charge transfer resistance of HGCNs. This results from the better conductivity of HGCN, in good agreement with the results of the Mott–Schottky tests. Furthermore, no decrease in the H_2 production rate was observed during a longtime photocatalytic measurement (Figure 5D; Figure S6, Supporting Information), implying the good stability of HGCN. This is confirmed by the very stable transient photocurrent after seven on–off cycles of intermittent irradiation (Figure 5D). This may be the result of the holey nanosheet structure of HGCNs because of the large decrease in the π–π stacking and van der Waals interaction of nanosheets due to the abundant in-plane holes. These holes are still found in the TEM images after the photocatalytic process (Figure S7, Supporting Information), suggesting their good cyclic performance.

3. Conclusion

In conclusion, HGCNs containing a large number of carbon vacancies were prepared by heating BGCN under an NH_3 atmosphere. The NH_3 etching not only helps to exfoliate the BGCN into nanosheets with abundant in-plane holes producing a high specific surface area of 196 m^2 g^{-1}, but also produces carbon vacancies without significantly changing the chemical structure. Compared to BGCN, HGCNs exhibit an ≈20 times higher photocatalytic activity for hydrogen production under visible light as a result of the holey structure, a higher accessible SSA, better light absorption, a higher donor density, and a remarkably increased separation efficiency of photoexcited electrons and holes. The excellent photocatalytic performance indicates that the material may be used as an efficient and sustainable photocatalyst for alleviating global environmental and energy issues.

Supporting Information

Supporting Information is available from the Wiley Online Library or from the author.

Acknowledgements

This work was financially supported by the National Basic Research Program of China (2014CB932400), the National Natural Science Foundation of China (Grant Nos. 51302274, 51372167, and U1401243), and the Shenzhen Basic Research Project (Grant No. ZDSYS20140509172959981). The authors also acknowledge financial support from the Guangdong Province Innovation R&D Team Plan (Grant No. 2009010025).

Received: August 3, 2015
Revised: September 2, 2015
Published online: October 15, 2015

[1] a) Y. Qu, X. Duan, *Chem. Soc. Rev.* **2013**, *42*, 2568; b) J. Ran, J. Zhang, J. Yu, M. Jaroniec, S. Z. Qiao, *Chem. Soc. Rev.* **2014**, *43*, 7787; c) X. C. Wang, K. Maeda, A. Thomas, K. Takanabe, G. Xin, J. M. Carlsson, K. Domen, M. Antonietti, *Nat. Mater.* **2009**, *8*, 76; d) J. Liu, Y. Liu, N. Liu, Y. Han, X. Zhang, H. Huang, Y. Lifshitz, S.-T. Lee, J. Zhong, Z. Kang, *Science* **2015**, *347*, 970; e) Y.-S. Jun, E. Z. Lee, X. Wang, W. H. Hong, G. D. Stucky, A. Thomas, *Adv. Funct. Mater.* **2013**, *23*, 3661; f) R. Marschall, *Adv. Funct. Mater.* **2014**, *24*, 2421; g) P. Niu, L. Zhang, G. Liu, H.-M. Cheng, *Adv. Funct. Mater.* **2012**, *22*, 4763.

[2] Y. Kim, D. Shin, W. J. Chang, H. L. Jang, C. W. Lee, H.-E. Lee, K. T. Nam, *Adv. Funct. Mater.* **2015**, *25*, 2369.

[3] a) S. Cao, J. Low, J. Yu, M. Jaroniec, *Adv. Mater.* **2015**, *27*, 2150; b) Y. Gong, M. Li, Y. Wang, *ChemSusChem* **2015**, *8*, 931; c) Y. Zheng, J. Liu, J. Liang, M. Jaroniec, S. Z. Qiao, *Energ. Environ. Sci.* **2012**, *5*, 6717; d) X. Wang, S. Blechert, M. Antonietti, *ACS Catal.* **2012**, *2*, 1596; e) Z. Zhao, Y. Sun, F. Dong, *Nanoscale* **2015**, *7*, 15; f) Y. Wang, X. Wang, M. Antonietti, *Angew. Chem. Int. Ed.* **2012**, *51*, 68.

[4] a) M. K. Bhunia, K. Yamauchi, K. Takanabe, *Angew. Chem. Int. Ed.* **2014**, *53*, 11001; b) X. Zhang, L. Yu, C. Zhuang, T. Peng, R. Li, X. Li, *ACS Catal.* **2013**, *4*, 162; c) M. Zhang, X. Wang, *Energ. Environ. Sci.* **2014**, *6*, 1902.

[5] a) Z. Lin, X. Wang, *Angew. Chem. Int. Ed.* **2013**, *52*, 1735; b) J. S. Zhang, J. H. Sun, K. Maeda, K. Domen, P. Liu, M. Antonietti, X. Z. Fu, X. C. Wang, *Energ. Environ. Sci.* **2011**, *4*, 675.

[6] P. Niu, L.-C. Yin, Y.-Q. Yang, G. Liu, H.-M. Cheng, *Adv. Mater.* **2014**, *26*, 8046.

[7] a) C. Chang, L. Zhu, S. Wang, X. Chu, L. Yue, *ACS Appl. Mat. Interfaces* **2014**, *6*, 5083; b) Y. Hou, F. Zuo, A. P. Dagg, J. Liu, P. Feng, *Adv. Mater.* **2014**, *26*, 5043; c) Y. Hou, A. B. Laursen, J. Zhang, G. Zhang, Y. Zhu, X. Wang, S. Dahl, I. Chorkendorff, *Angew. Chem.*

Int. Ed. **2013**, *52*, 3621; d) H. Li, J. Liu, W. Hou, N. Du, R. Zhang, X. Tao, *Appl. Catal. B* **2014**, *160*, 89; e) X. Yao, X. Liu, X. Hu, *ChemCatChem* **2014**, *6*, 3409; f) Y. Wang, R. Shi, J. Lin, Y. Zhu, *Energ. Environ. Sci.* **2011**, *4*, 2922.

[8] a) M. Groenewolt, M. Antonietti, *Adv. Mater.* **2005**, *17*, 1789; b) X. Jin, V. V. Balasubramanian, S. T. Selvan, D. P. Sawant, M. A. Chari, G. Q. Lu, A. Vinu, *Angew. Chem.* **2009**, *121*, 8024.

[9] a) Y. Hou, Z. Wen, S. Cui, X. Guo, J. Chen, *Adv. Mater.* **2013**, *25*, 6291; b) S. Yang, Y. Gong, J. Zhang, L. Zhan, L. Ma, Z. Fang, R. Vajtai, X. Wang, P. M. Ajayan, *Adv. Mater.* **2013**, *25*, 2452; c) X. Zhang, X. Xie, H. Wang, J. Zhang, B. Pan, Y. Xie, *J. Am. Chem. Soc.* **2012**, *135*, 18; d) J. Hong, S. Yin, Y. Pan, J. Han, T. Zhou, R. Xu, *Nanoscale* **2014**, *6*, 14984; e) Y. Li, L. Fang, R. Jin, Y. Yang, X. Fang, Y. Xing, S. Song, *Nanoscale* **2015**, *7*, 758; f) J. Tian, Q. Liu, C. Ge, Z. Xing, A. M. Asiri, A. O. Al-Youbi, X. Sun, *Nanoscale* **2013**, *5*, 8921.

[10] a) X. Bai, L. Wang, R. Zong, Y. Zhu, *J. Phys. Chem. C* **2013**, *117*, 9952; b) X. H. Li, X. C. Wang, M. Antonietti, *Chem. Sci.* **2012**, *3*, 2170.

[11] Y. Zhao, F. Zhao, X. Wang, C. Xu, Z. Zhang, G. Shi, L. Qu, *Angew. Chem. Int. Ed.* **2014**, *53*, 13934.

[12] a) Q. Guo, Y. Xie, X. Wang, S. Zhang, T. Hou, S. Lv, *Chem. Commun.* **2004**, *1*, 26; b) Y. Gong, J. Wang, Z. Wei, P. Zhang, H. Li, Y. Wang, *ChemSusChem* **2014**, *7*, 2303.

[13] D. Zheng, C. Huang, X. Wang, *Nanoscale* **2015**, *7*, 465.

[14] a) Q. Han, B. Wang, Y. Zhao, C. Hu, L. Qu, *Angew. Chem.* **2015**, *127*, 11595; b) Q. Han, B. Wang, Y. Zhao, C. Hu, L. Qu, *Angew. Chem. Int. Ed.* **2015**, *54*, 11433.

[15] a) S. Yang, X. Feng, X. Wang, K. Müllen, *Angew. Chem. Int. Ed.* **2011**, *50*, 5339; b) T. Y. Ma, S. Dai, M. Jaroniec, S. Z. Qiao, *Angew. Chem. Int. Ed.* **2014**, *53*, 7281; c) Y. Tang, P. Wang, J.-H. Yun, R. Amal, Y. H. Ng, *J. Mater. Chem. A* **2015**, *3*, 15876.

[16] a) Y. Hou, J. Li, Z. Wen, S. Cui, C. Yuan, J. Chen, *Nano Energy* **2014**, *8*, 157; b) Q. Liang, Z. Li, X. Yu, Z.-H. Huang, F. Kang, Q.-H. Yang, *Adv. Mater.* **2015**, *27*, 4634.

[17] a) X. Han, M. R. Funk, F. Shen, Y.-C. Chen, Y. Li, C. J. Campbell, J. Dai, X. Yang, J.-W. Kim, Y. Liao, J. W. Connell, V. Barone, Z. Chen, Y. Lin, L. Hu, *ACS Nano* **2014**, *8*, 8255; b) X. Zhao, C. M. Hayner, M. C. Kung, H. H. Kung, *ACS Nano* **2011**, *5*, 8739; c) Z. Xiang, D. Cao, L. Huang, J. Shui, M. Wang, L. Dai, *Adv. Mater.* **2014**, *26*, 3315; d) X.-H. Li, M. Antonietti, *Angew. Chem. Int. Ed.* **2013**, *52*, 4572; e) Y.-Y. Peng, Y.-M. Liu, J.-K. Chang, C.-H. Wu, M.-D. Ger, N.-W. Pu, C.-L. Chang, *Carbon* **2015**, *81*, 347; f) Z.-J. Jiang, Z. Jiang, W. Chen, *J. Power Sources* **2014**, *251*, 55; g) Z. Xing, J. Tian, Q. Liu, A. M. Asiri, P. Jiang, X. Sun, *Nanoscale* **2014**, *6*, 11659; h) Y. Xu, Z. Lin, X. Zhong, X. Huang, N. O. Weiss, Y. Huang, X. Duan, *Nat. Commun.* **2014**, *5*, 4554.

[18] T. Y. Ma, Y. Tang, S. Dai, S. Z. Qiao, *Small* **2014**, *10*, 2382.

[19] a) Z. Zhao, Y. Dai, J. Lin, G. Wang, *Chem. Mater.* **2014**, *26*, 3151; b) Y. Wang, J. S. Zhang, X. C. Wang, M. Antonietti, H. R. Li, *Angew. Chem. Int. Ed.* **2010**, *49*, 3356.

[20] Y. Kang, Y. Yang, L.-C. Yin, X. Kang, G. Liu, H.-M. Cheng, *Adv. Mater.* **2015**, *27*, 4572.

[21] J. Zhang, M. Zhang, C. Yang, X. Wang, *Adv. Mater.* **2014**, *26*, 4121.

[22] J. Zhang, M. Zhang, L. Lin, X. Wang, *Angew. Chem. Int. Ed.* **2015**, *54*, 6297.

[23] W. Luo, B. Wang, C. G. Heron, M. J. Allen, J. Morre, C. S. Maier, W. F. Stickle, X. Ji, *Nano Lett.* **2014**, *14*, 2225.

[24] G. Zhang, M. Zhang, X. Ye, X. Qiu, S. Lin, X. Wang, *Adv. Mater.* **2014**, *26*, 805.

[25] D. Gao, Q. Xu, D. Xue, M. Si, J. Zhang, Z. Yan, Z. Yang, *Nanoscale* **2014**, *6*, 2577.

[26] a) M. Shalom, M. Guttentag, C. Fettkenhauer, S. Inal, D. Neher, A. Llobet, M. Antonietti, *Chem. Mater.* **2014**, *26*, 5812; b) X. Li, G. Hartley, A. J. Ward, P. A. Young, A. F. Masters, T. Maschmeyer, *J. Phys. Chem. C* **2015**, *119*, 14938.

[27] a) Y. Zheng, L. Lin, X. Ye, F. Guo, X. Wang, *Angew. Chem. Int. Ed.* **2014**, *53*, 11926; b) G. Liu, P. Niu, C. H. Sun, S. C. Smith, Z. G. Chen, G. Q. Lu, H. M. Cheng, *J. Am. Chem. Soc.* **2010**, *132*, 11642.

[28] Y. Cao, Z. Zhang, J. Long, J. Liang, H. Lin, H. Lin, X. Wang, *J. Mater. Chem. A* **2014**, *2*, 17797.

[29] W. Zhou, W. Li, J.-Q. Wang, Y. Qu, Y. Yang, Y. Xie, K. Zhang, L. Wang, H. Fu, D. Zhao, *J. Am. Chem. Soc.* **2014**, *136*, 9280.